

Novel Stimuli-Responsive Turbostratic Oxides/Hydroxides for Material-Driven Robots

Kin Wa Kwan, Runni Wu, Wenrui Ma, and Alfonso H. W. Ngan*


Herein, a novel class of high-performing actuating oxides/hydroxides with turbostratic crystal structures is reviewed. These materials, including nickel hydroxide/oxyhydroxide, cobalt oxides/hydroxides, nickel-doped cobalt oxides/hydroxides, and manganese oxides, exhibit a volume-changing redox reaction, rendering them an electrochemical actuation behavior. Also, due to their turbostratic crystal structures, they typically exhibit light-driven actuation due to water deintercalation from the crystal structure induced by light. Compared with other actuating materials, these oxides/hydroxides actuate with high stress and strain at fast rates, under very low stimuli requirements. Furthermore, they are easily printable on different substrates, thus allowing flexible robots with demodularized muscle-skeletal designs to be made.

1. Introduction

1.1. The Demodularized Muscle-Skeletal Approach to Robotics

Robots are traditionally conceived as devices that mimic the muscle-skeletal constructs of humans or animals, in which load-bearing members are moved by prime movers. Humanoid-scale robots are often constructed with modularized skeletal elements moved by motors at localized power points, thus resulting in motions which, although easily programmable, are limiting in terms of degrees of freedom. Not only in humans or large animals are the muscle-skeletal structure much less well defined and localized, but for robots in the insect scale, such a structure may become very limiting, as conventional prime movers such as electric, hydraulic, or pneumatic motors would be too big to be deployed. Robotic design will therefore benefit from a more general approach in which the muscle-skeletal structure is made demodularized and smoothly distributed in an optimized way to enable complex, multimorphic motions.

Dr. K. W. Kwan, Dr. R. Wu, W. Ma, Prof. A. H. W. Ngan
Department of Mechanical Engineering
The University of Hong Kong
Pokfulam Road, Hong Kong, P. R. China
E-mail: hwngan@hku.hk

 The ORCID identification number(s) for the author(s) of this article can be found under <https://doi.org/10.1002/aisy.202000215>.

© 2021 The Authors. Advanced Intelligent Systems published by Wiley-VCH GmbH. This is an open access article under the terms of the Creative Commons Attribution License, which permits use, distribution and reproduction in any medium, provided the original work is properly cited.

DOI: 10.1002/aisy.202000215

1.2. Stimuli-Responsive Actuating Materials

As shown in Table 1 and Figure 1, a number of actuating materials have been developed which can be used to drive insect-scale robots using the abovementioned demodularized muscle-skeletal approach. Piezoelectric ceramics or polymers^[1–7] are responsive to high electric fields on the order of MV m^{-1} to induce movements of charge centers to cause straining in a “dry” environment (Figure 1a). Dielectric elastomers are passive dielectric films strainable by the electrostatic force between a pair of sandwiching electrodes.^[8–12] Other actuating

materials responsive to electrical signals require a “wet” electrochemical environment to operate: conducting polymers^[13–17] rely on a redox reaction in an electrolytic environment to induce ionic transport within the material to produce straining (Figure 1b), and nanostructured carbon materials [carbon nanotubes (CNTs) and graphene]^[18–31] and noble metals^[32–36] also actuate in a liquid electrolyte by virtue of electric double-layer formation on the solid wall to induce straining of the latter (Figure 1c). In addition to electrical or electrochemical stimuli, other materials are responsive to water/humidity, heat, or light. Water-absorbing materials such as hydrogels^[37–40] or cellulose materials^[41] swell by uptake of water, although with very slow response rates. In terms of heat stimuli, shape-memory polymers^[42–46] are “trained” by mechanical stretching above the glass-transition temperature followed by cooling below it to produce a metastable low-entropy state, and “actuation” is by reheating the polymer to above the glass transition to recover the original high-entropy shape (Figure 1d). Heat-induced actuation is also conveniently achievable in a composite system with components of different thermal expansivities, where a heat stimulus will produce thermal-mismatch straining of the composite.^[47–51] A response to light is often achieved via a photo-coupled effect with the mechanisms mentioned earlier; for example, photostrictive piezoelectric materials rely on a photovoltaic effect in the material system to generate the electric field required by the piezoelectric effect to produce actuation.^[52,53] Similarly, the photothermal response of a material component in a composite system can be used to induce thermal mismatch straining upon receiving light stimulation.^[47,48] Liquid-crystal elastomers are a class of actuating materials that are multistimuli responsive; here, straining is due to alignment/dealignment of the liquid crystals which form an intrinsic part of the polymer network, and such reorganization can be induced by temperature (Figure 1e), electric field, or

Table 1. Stimuli-responsive actuating materials.

Materials	Mechanism	Advantages	Limitations	References
Piezoelectric ceramics	Electric field induced straining in crystal without inversion symmetry	Rate response > 10% s ⁻¹ , strains ≈0.1%, stress in tens of MPa As for piezoelectric	High triggering voltages in kV range	[1-3]
Photostrictive piezoelectric ceramics	Photovoltaic plus piezoelectric effects		High light intensity of >500 mW cm ⁻² required	[52,53]
Dielectric elastomers	Passive dielectric elastomer strained by electrostatic pressure	Rate response > 10% s ⁻¹ , strains >10%	High operating voltages in kV range	[8-12]
Piezoelectric polymers	Piezoelectric effect in polymers with polarized crystalline phases	Large strain ≈10% and response rate >1% s ⁻¹	High electric field ≈MV m ⁻¹ needed	[4-7]
Conducting polymers	Redox induced ionic transport to and from polymer chains resulting in volume change	Strain >1%, operating voltage a few volts, stress in tens of MPa	Slow response rate of ≪1% s ⁻¹	[13-17]
Shape memory polymers	Deformation above glass-transition temperature T _g leads to low-entropy state metastabilizable by cooling to below T _g ; on reheating to >T _g , the original high-entropy state is recovered. Instead of cooling/heating, the low-entropy state can also be meta-stabilized by photocross-linking to raise the T _g , and shape recovery by photoinduced cleaving of the cross-linking to lower the T _g	Large strain >10%	Slow recovery response >10 s. Shape-memory effect can be irreversible.	[42-46]
Hydrogels	Water intercalation into gel structure causing swelling			
Liquid crystal elastomers	Alignment/dealignment and/or self-organization of liquid crystals induced by temperature change, electric field, or light, causing straining	Large strain >10%	Slow response from several minutes to hours	[37-40]
Carbon nanotubes/graphene/graphene oxides based materials	Electrochemical actuation due to quantum chemical straining due to double-layer charging. Also, thermal/electrothermal expansion	High strain >10%	For light actuation, high-intensity UV light is required	[54-59]
Nanoporous noble metals	Surface stress induced by electric double layer in liquid electrolyte environment	Operating at a few volts, ≈1% strain, fast response at >10% s ⁻¹	–	[18-31]
Composite systems	Very often, these rely on thermal mismatch between components: e.g., ink/polyethylene terephthalate (PET)/CNT trilayered composite responsive to electricity, near-infrared (NIR) light, humidity, and volatile organic vapors: ink layer exhibits volume expansion upon heating, exposure to moisture/vapors and NIR absorption; PET as passive layer; CNT film for electroheating due to its electrical resistance. e.g., wax-filled CNT yarn: paraffin wax as yarn guest undergoes thermal expansion from direct heating, or electro/photothermal heating.	Operating at ≈1 V, strain at ≈0.1%	Slow response of ≪0.1% s ⁻¹	[32-36]
Turbostratic oxides/hydroxides	Electrochemical actuation due to volume-changing redox reaction. Light actuation due to water deintercalation from turbostratic crystal structure.	–	For light actuation, IR or high-intensity NIR light is needed	[47,48]
		Operating at low stimuli requirements: <1 V for electrochemical actuation, <1 sun intensities for light actuation in the visible range. Good stress (tens of MPa), good intrinsic strain ≈1%, Fast response <1 s. Low cost, printable.	–	[61-63,65-68,72]

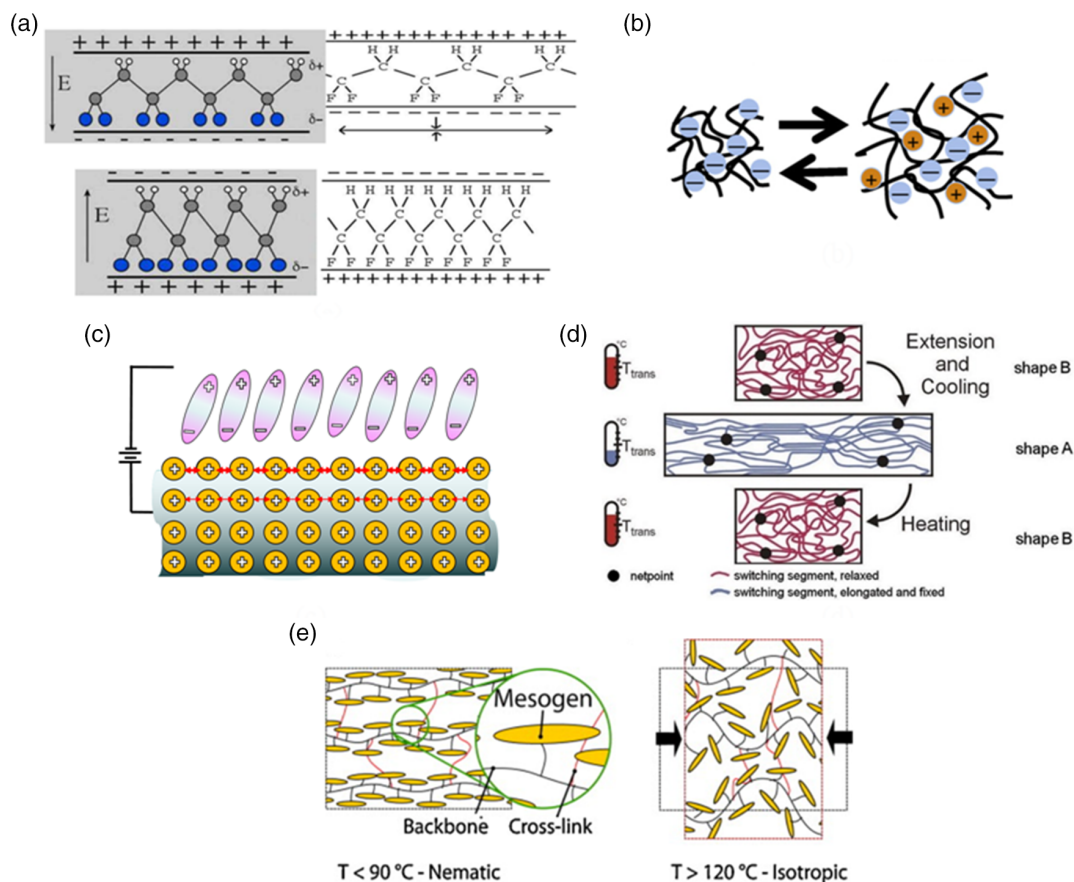


Figure 1. Mechanisms of various actuation materials. a) Piezoelectric β -crytalline polyvinylidene fluoride $-(C_2H_2F_2)_n-$ with polarized molecular chains: an electric field antiparallel to the molecular polar direction thins and lengthens the chain, and vice versa. Reproduced with permission.^[7] Copyright 2017, American Institute of Physics. b) Conducting polymer: redox induces ion insertion and deinsertion to cause volume change. Adapted with permission.^[17] Copyright 2012, Elsevier. c) Electric dipole layer (EDL)-induced actuation: when a clean metal is positively charged in a liquid electrolyte, EDL forms to drive away free electrons from the metal surface. Internuclear repulsion in surface causes the metal bulk to expand. d) Shape memory polymer: mechanical deformation at above glass-transition temperature T_g aligns the molecules and lowers the entropy, then cooling to below T_g retains this low-entropy configuration as a metastable state; reheating to above T_g recovers the original shape with high entropy. Reproduced with permission.^[43] Copyright 2007, Elsevier. e) Liquid-crystal elastomer: temperature change induces liquid-crystal alignment/dealignment causing straining. Reproduced with permission.^[56] Copyright 2015, Elsevier.

light.^[54–59] Magnetic field is also a well-known form of stimuli for moving powders of ferromagnetic materials, which can then be used to drive small robots into which they are embedded.^[60] However, of the various stimuli surveyed here, heat/temperature, water/humidity, and magnetic field are less easily delivered to compact robots than electrical or light signals.

1.3. Turbostratic Oxides/Hydroxides

This article reviews a new class of high-performing actuating metal oxides/hydroxides with crystal structures that are “turbostratic” (Figure 2a), e.g., nickel hydroxide and oxyhydroxide. Compared with the actuating materials in Table 1, these oxides/hydroxides exhibit two distinct actuation mechanisms simultaneously (Figure 2). The first arises from their turbostratic crystal structures into which water molecules are normally intercalated (Figure 2a), and on receiving stimuli such as light, heat, or reduced environmental humidity, deintercalation of water from the crystal structure results in large contractive strains.^[61]

The second actuation mechanism^[62,63] is a volume-changing redox reaction in an electrolytic environment (Figure 2b,c). These two mechanisms render such materials multiresponsive to various stimuli, including electrical, light, heat, and humidity signals in both “dry” and “wet” environments. Another significant advantage of these oxides/hydroxides is that they are easily electrochemically printable on different substrates at low costs, and so they can be integrated within a flexible robot body in tailor-made distribution, to realize the aforementioned demodularized muscle-skeletal approach for achieving multi-morphic shape changes. In the following, the microstructure and actuation responses of this family of actuating oxides/hydroxides are first reviewed, followed by the engineering means for making robotic devices.

2. Turbostratic Oxides/hydroxides

This class of newly discovered actuating materials has a number of attractive properties over the existing materials, as shown in

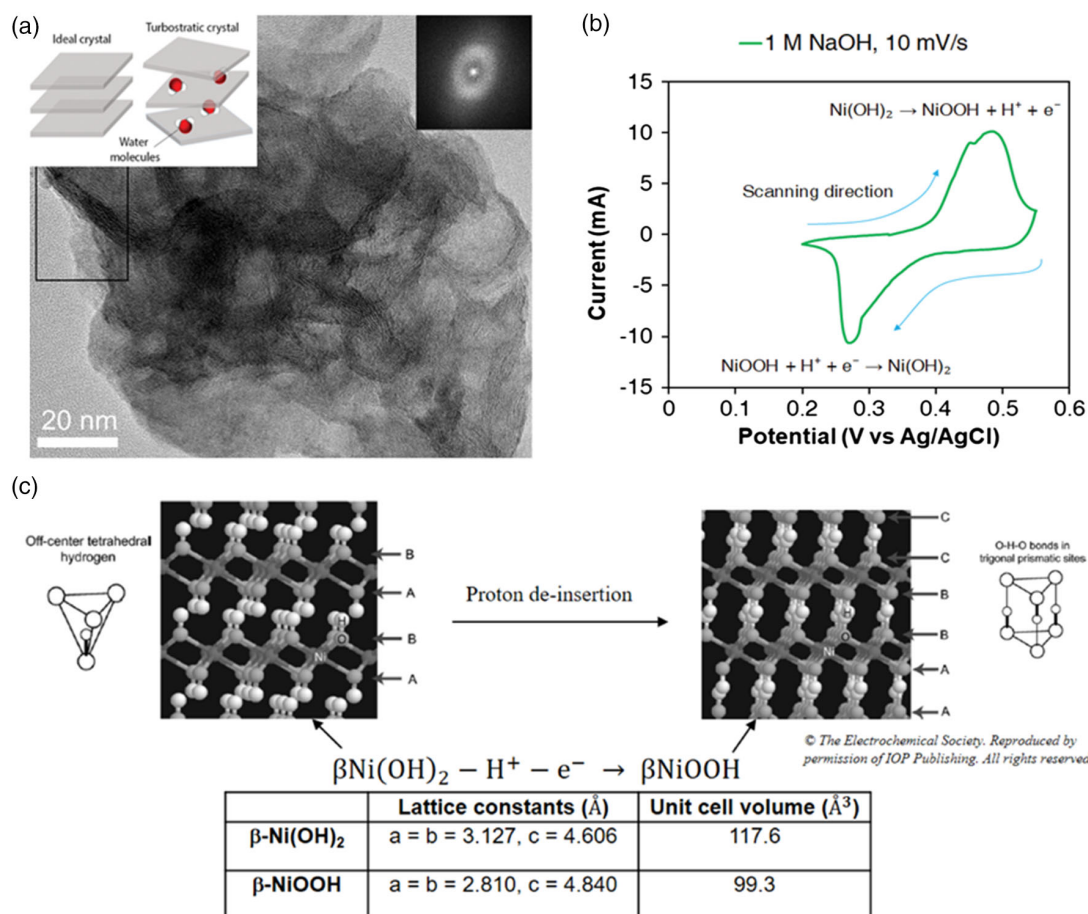


Figure 2. Actuation mechanisms in turbostratic Ni(OH)₂/NiOOH (NHO). a) Electron micrograph showing the turbostratic crystal structure of Ni(OH)₂, into which water molecules are intercalated in ambient conditions. Light, heat, and decreased environmental humidity cause water removal and shrinkage strain. Reproduced with permission.^[69] Copyright 2018, Wiley-VCH. b,c) Oxidation of Ni(OH)₂ by proton deinsertion results in NiOOH phase with reduced crystal volume, and vice versa. b) Cyclic voltammogram of Ni(OH)₂/NiOOH 1 M NaOH. Reproduced with permission.^[61] Copyright 2018, American Association for the Advancement of Science. c) Crystal structures (Adapted with permission.^[74] Copyright 2016, IOP publishing Ltd.), and lattice constants^[75,76] of $\beta\text{-Ni(OH)}_2$ and $\beta\text{-NiOOH}$ phases in the redox reaction.

Table 1. **Table 2** shows the material systems studied to-date, which are abbreviated as NHO, COH, CNH, and MnO_x hereafter. Of these, the NHO denoting the Ni(OH)₂/NiOOH redox couple is used here as a prototypic system for discussion.

2.1. Volume-Changing Redox in NHO

The $\beta\text{-Ni(OH)}_2$ phase of the NHO system has a hexagonal crystal structure, in which the (001) basal planes are outlined by layers of the Ni—O—H groups (Figure 2c). On oxidation, the $\beta\text{-Ni(OH)}_2$

phase transforms into the $\beta\text{-NiOOH}$ phase, in which every pair of the previous O—H groups in adjacent (001) basal planes of the $\beta\text{-Ni(OH)}_2$ structure join to form a single O—H—O group following the deinsertion of a proton. This process results in a stretching of the structure along the *c*-axis but contraction on the basal plane, with an overall volume reduction of about 15%, or a linear strain of about 5%. The oxidation happens at a low potential difference of about 0.45 V relative to Ag/AgCl electrode, and reduction back to the $\beta\text{-Ni(OH)}_2$ phase occurs at about 0.3 V (Figure 2b); thus, the volume switching can be made to occur within a narrow potential window of much less

Table 2. Stimuli-responsive turbostratic oxides/hydroxides.

Abbreviation	Material system	Actuation behavior	References
NHO	Ni(OH) ₂ /NiOOH	Electrochemical, light	[61-63]
COH	Mixture of Co(OH) ₂ , CoOOH, Co ₃ O ₄ and CoO ₂ phases	Electrochemical, light	[65,67]
CNH	Nickel doped COH	Electrochemical, light	[67]
MnO _x	MnO _x	Electrochemical only	[66,68]

than 1 V, which is a significant advantage over piezoelectric and dielectric materials which require kilo-volts to operate (Table 1). The low operating potential for NHO is evidently due to the easy insertion/deinsertion of proton in the phase transition.

2.2. Turbostratic Crystal Structure in NHO

The crystal structures shown in Figure 2c are only the ideal structures for the NHO system, and the actuation strains due to electrochemical stimulation are far less than the abovementioned $\approx 5\%$ for the ideal structures of $\beta\text{-Ni(OH)}_2$ and $\beta\text{-NiOOH}$.^[63] In practice, the lattice fringes seen in a high-resolution transmission electron image of the $\beta\text{-Ni(OH)}_2$ phase (Figure 2a) are wavy, indicative of the turbostratic character, in which the crystal planes, especially the (001) basal planes, are misaligned due to water intercalation, as shown in the inset in Figure 2a. Furthermore, the (001) peak in the X-ray diffraction (XRD) pattern (especially the reduced state in Figure 3a) is broad, which is believed to be a textured feature of turbostratic layered hydroxides with finite and random thicknesses of crystalline slabs perpendicular to the *c*-axis intercalated with ions.^[64] Comparing the XRD patterns of the reduced, $\beta\text{-Ni(OH)}_2$ -rich state (blue curves) and the oxidized, $\beta\text{-NiOOH}$ -rich state (black curves) in Figure 3a, b, on oxidation, the (100) peak of the $\beta\text{-Ni(OH)}_2$ phase vanishes while the (101) of the $\beta\text{-NiOOH}$ appears, due to the shear along the basal planes accompanying the joining of two O—H groups

into a single O—H—O group as mentioned earlier (Figure 2c). Another change in the XRD on oxidation is the sharpening of the (001) peak, which is also likely due to the increased crystal thickness along the *c*-axis.^[64]

2.3. Light Stimulated Response in NHO

On light stimulation, NHO exhibits shrinkage (Figure 4a) only in normal-humidity environments but not in vacuum.^[65] Furthermore, the material also contracts as it is heated, or as the environmental humidity is reduced.^[65] As shown in Figure 3a, b, in situ light stimulation in the X-ray diffractometer does not alter the intensities of the peaks, and so the light-induced actuation is not due to a phase change. Rather, as shown in Figure 3c, on light stimulation (red curve), the (001) broad peak undergoes asymmetrical broadening toward the right side, indicating collapse of the (001) lattice spacing. This suggests that light induces water deintercalation from the crystal structure, and explains the contractive response on light stimulation. In Figure 3c, the light stimulation only causes the right half of the (001) peak to right-broaden, while the left half is not affected. This is likely due to the small penetration depth of the visible light, so that only the top-surface layer of the sample, in which the (001) spacing is smaller due to dehydration, is stimulated by the light, while the deeper material with more water intercalated and hence larger (001) spacing is not triggered by the light.^[66]

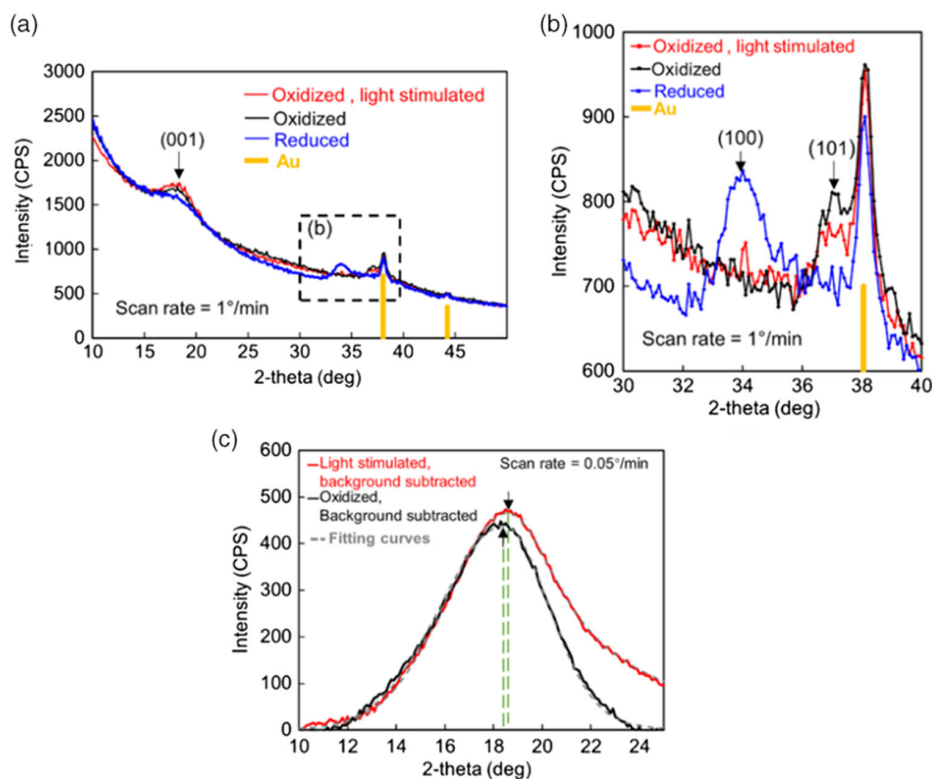


Figure 3. Stimuli-responsive microstructural changes in $\text{Ni(OH)}_2/\text{NiOOH}$ (NHO). a, b) XRD spectra under in situ light stimulation in the oxidized state (red), and oxidized (black) and reduced (blue) states without light stimulation. c) XRD spectra (background subtracted) of the oxidized state under in situ light stimulation (red), and without light stimulation (black). Extra peaks due to the Au substrates are labeled. Adapted with permission.^[66] Copyright 2020, Elsevier.

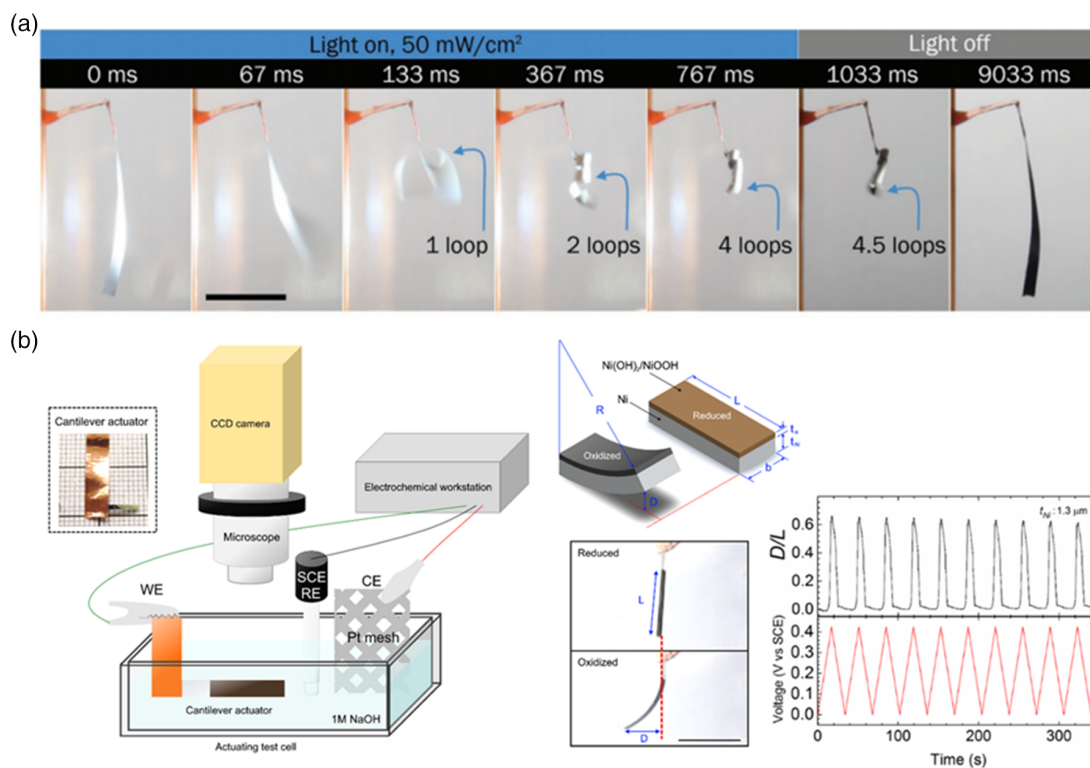


Figure 4. Typical actuation responses in turbostratic oxides/hydroxides. a) Light-triggered fast actuation response in COH (scale bar = 10 mm). Reproduced with permission.^[65] Copyright 2019, Wiley-VCH. b) Electrochemical actuation in NHO with the typical electrochemical setup for the actuation tests, and appearance of actuator in reduced and oxidized states (scale bar = 5 mm). Adapted with permission.^[63] Copyright 2017, Elsevier.

2.4. Other Oxides/hydroxides

Apart from the NHO system, COH and MnO_x are the only two other systems reported to exhibit electrochemical and/or light actuation.^[65–68] COH is a mixture of cobalt oxides (CoO_x) and hydroxides ($\text{Co}(\text{OH})_y$)^[65,67] with similar turbostraticity in their crystal structures as NHO. The COH system exhibits both electrochemical and light actuation,^[67] and its light-induced actuation is intrinsically better than that of NHO (see Figure 6b and discussion in Section 3). MnO_x is known to exhibit only electrochemical but not light actuation.^[66,68]

2.5. Composite Systems

In general, it may be possible to improve the actuation performance by forming composites between the individual oxide/hydroxide systems. For example, nickel doping into COH, to obtain the CNH system in Table 2, is found to significantly improve the stability of the light actuation, compared with both the individual NHO and COH systems.^[67] As mentioned earlier, the light actuation is due to light-induced water deintercalation from the turbostratic crystal structure, but if and when the turbostratic structure crystallizes,^[69] the light actuation behavior will be lost. In the CNH system, nickel doping into COH retards the crystallization of COH,^[70,71] and accordingly, the stability of the actuation is improved.^[67]

3. Chemomechanics

3.1. Bimorph Actuators

The basic construct involving turbostratic oxides/hydroxides in material-driven robots is a bimorph configuration comprising a thin layer of the active material (thickness h_a , Young modulus E_a) coated on top of a passive layer (thickness h_s , Young modulus E_s), as shown in Figure 5a. The reason for this choice is twofold. First, although the active material typically has a limited actuation strain on the order of 1% (see Figure 4a), large bending curvature on the order of 1 mm^{-1} can be achieved in the bimorph configuration (see Figure 7b), as will be explained later. Also, in terms of fabrication, the turbostratic oxides/hydroxides are conveniently electrodeposited on substrates, so the bimorph structure is natural. The bimorph configuration is not limited to the active layer being a uniformly coated layer on the substrate, but can be in a patterned form to achieve complex actuation motion (see Section 4).

3.2. Theory

Figure 5a show a bimorph cantilever actuator stimulated at the top surface of the active layer.^[65] The active material is quite generally representable by a mixture of an expanded and a contracted state in chemical equilibrium

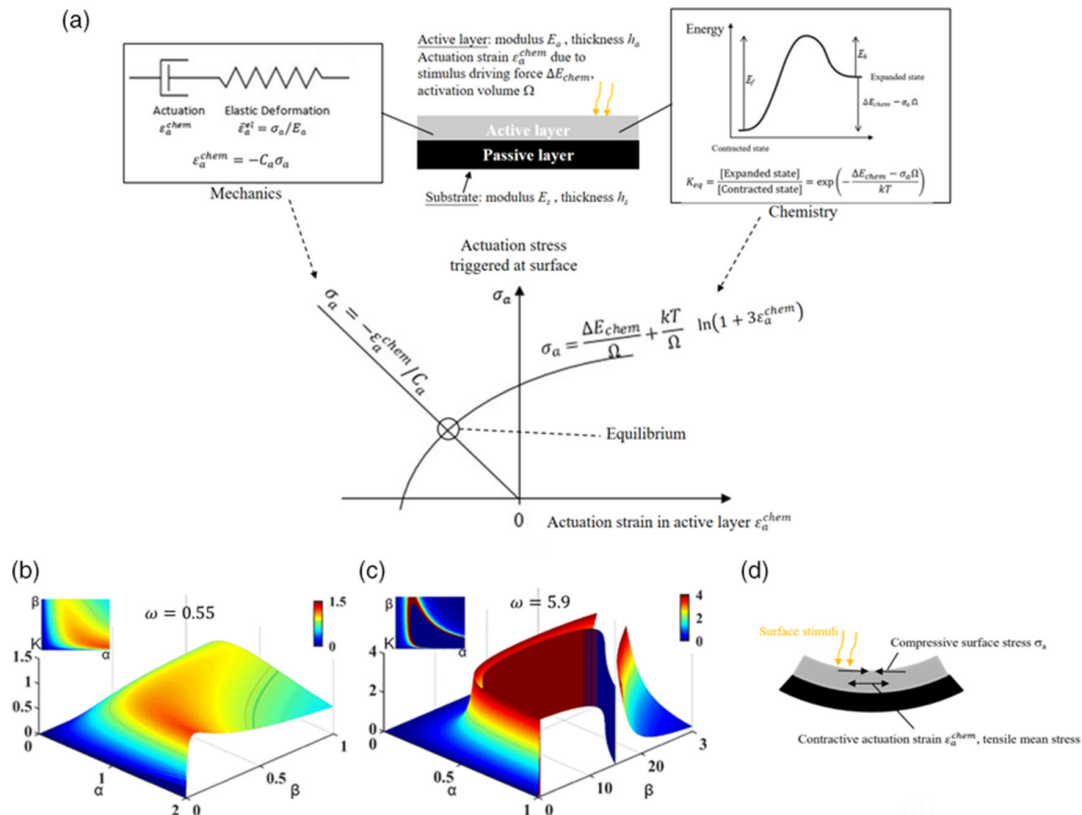


Figure 5. a) Chemomechanical equilibrium of surface-triggered bimorph actuator. Adapted with permission.^[65] Copyright 2019, Wiley-VCH. Surface stimuli induces a plastic actuation strain ϵ_a^{chem} within the active layer to bend the bimorph actuator, thus setting up a surface stress $\sigma_a = -\epsilon_a^{\text{chem}}/C_a$ at mechanical equilibrium. At chemical equilibrium, reaction constant K_{eq} is affected by the surface stress σ_a , and dictates the volumetric strain $3\epsilon_a^{\text{chem}}$. Simultaneous satisfaction of the two conditions gives the solution for σ_a and ϵ_a^{chem} . b,c) Plots of the $K(\alpha, \beta)$ surface for b) $\omega = 0.55$ and c) $\omega = 5.9$. d) Chemomechanical instability: a large contractive ϵ_a^{chem} within the active layer produces a compressive surface stress σ_a which further drives the active material toward the contractive state as $(\Delta E_{\text{chem}} - \sigma_a \Omega)$ increases. Unstable actuation with very large magnitude occurs when $\omega \geq 2$, as shown in the case in (c). b–d) Adapted with permission.^[72] Copyright 2020, Elsevier.

expanded state \rightleftharpoons contracted state (1)

The stimuli received at the surface induce a chemical force ΔE_{chem} to drive the aforementioned reaction toward the direction of the contracted state, but as the actuator bends, a local stress σ_a (positive if tensile) is set up at the surface which modifies the effective driving force to $(\Delta E_{\text{chem}} - \sigma_a \Omega)$, where Ω is the activation volume. Chemical equilibrium is therefore represented by

$$(1 + 3\epsilon_a^{\text{chem}}) \approx K_{\text{eq}} = \frac{[\text{Expanded state}]}{[\text{Contracted state}]} = \exp\left(-\frac{\Delta E_{\text{chem}} - \sigma_a \Omega}{kT}\right) \quad (2)$$

where the reaction constant K_{eq} defines the ratio of the equilibrium concentrations of the expanded and contracted states, and is therefore related to the volumetric strain $3\epsilon_a^{\text{chem}}$ of the active material (ϵ_a^{chem} =linear actuation strain). For small actuation, Equation (2) reduces to

$$\epsilon_a^{\text{chem}} \approx \left(\frac{\sigma_a}{E_a}\right) \omega - \phi \quad (3)$$

where $\phi = \Delta E_{\text{chem}}/(3kT)$, $\omega = E_a \Omega/(3kT)$, and kT is the thermal energy.

On the contrary, the actuation stress σ_a and strain ϵ_a^{chem} are also governed by the elasticity of the bimorph cantilever. As shown in Figure 5a, the actuation strain ϵ_a^{chem} is effectively a self, plastic strain within the active layer that deforms the bimorph cantilever in an elastic manner, and mechanics considerations^[65] lead to the following conditions for mechanical equilibrium

$$\sigma_a = -\epsilon_a^{\text{chem}}/C_a, C_a = \frac{(h_a + h_s) + \frac{E_a h_a^2 + E_s h_s^2}{6(h_a + h_s)} \left(\frac{1}{E_a h_a} + \frac{1}{E_s h_s}\right)}{\frac{E_a h_a^2 + E_s h_s^2}{6h_a(h_a + h_s)} - \frac{E_s h_s}{2}} \quad (4)$$

$$\kappa = -\frac{\epsilon_a^{\text{chem}}}{K_a}, K_a = \frac{(h_a + h_s)}{2} + \frac{E_a h_a^3 + E_s h_s^3}{6(h_a + h_s)} \left(\frac{1}{E_a h_a} + \frac{1}{E_s h_s}\right) \quad (5)$$

where κ is the equilibrium bending curvature of the cantilever. From Equation (2), (4), and (5), the equilibrium curvature κ is given in a normalized form as follows^[65]

$$\frac{\kappa h_s}{\phi \beta^{1/3}} = K(\alpha, \beta, \omega) \quad (6)$$

$$= \frac{6\alpha\beta^{2/3}(1+\alpha)}{(1+\alpha\beta)(1+\alpha^3\beta) + \omega[1-\alpha^2\beta(3+2\alpha)] + 3\alpha\beta(1+\alpha)^2}$$

where $\alpha = h_a/h_s$ and $\beta = E_a/E_s$. Plots of the $K(\alpha, \beta)$ surface for a small (0.55) and a large (5.9) value of ω are shown in Figure 5b,c. Equation (6) shows that, for the same thickness ratio α , modulus ratio β , and normalized activation volume ω , the bending curvature of the actuator κ is proportional to the normalized chemical driving force ϕ ; therefore, ϕ is an important figure of merit of the actuating material as used in a bimorph actuator.

3.3. Experimental Verification

Figure 6 shows experimental data supporting the aforementioned theory. Figure 6a shows data of σ_a and ϵ_a^{chem} for different bimorph actuator systems calculated from the experimental actuation curvature κ using Equation (4) and (5). The slopes and intercepts of the plots in Figure 6a enable the parameters

ω and ϕ to be evaluated according to Equation (3). Figure 6b shows the estimated ϕ for COH and NHO at different light intensities; it can be seen that COH has higher ϕ values than NHO, and so COH is an intrinsically higher performing actuating material than NHO. Finally, the normalized curvature K for different material systems is calculated from the experimental curvature κ as $K = \kappa h_s / \phi \beta^{1/3}$ according to the definition in Equation (6), and is plotted as discrete symbols in Figure 6c. The curves in Figure 6c show the theoretical trends $K(\alpha, \beta, \omega)$ according to Equation (6), which fit the experimental data well.

3.4. Summary

For surface-stimulated, bimorph cantilever actuators, an important figure of merit for the actuation performance of the active material is the normalized chemical driving force $\phi = \Delta E_{\text{chem}} / (3kT)$, which can be measured from the actuation strain ϵ_a^{chem} at zero actuation stress according to Equation (3) and Figure 6a. The actuation curvature κ of the bimorph actuator depends on the thicknesses and moduli of the active and passive

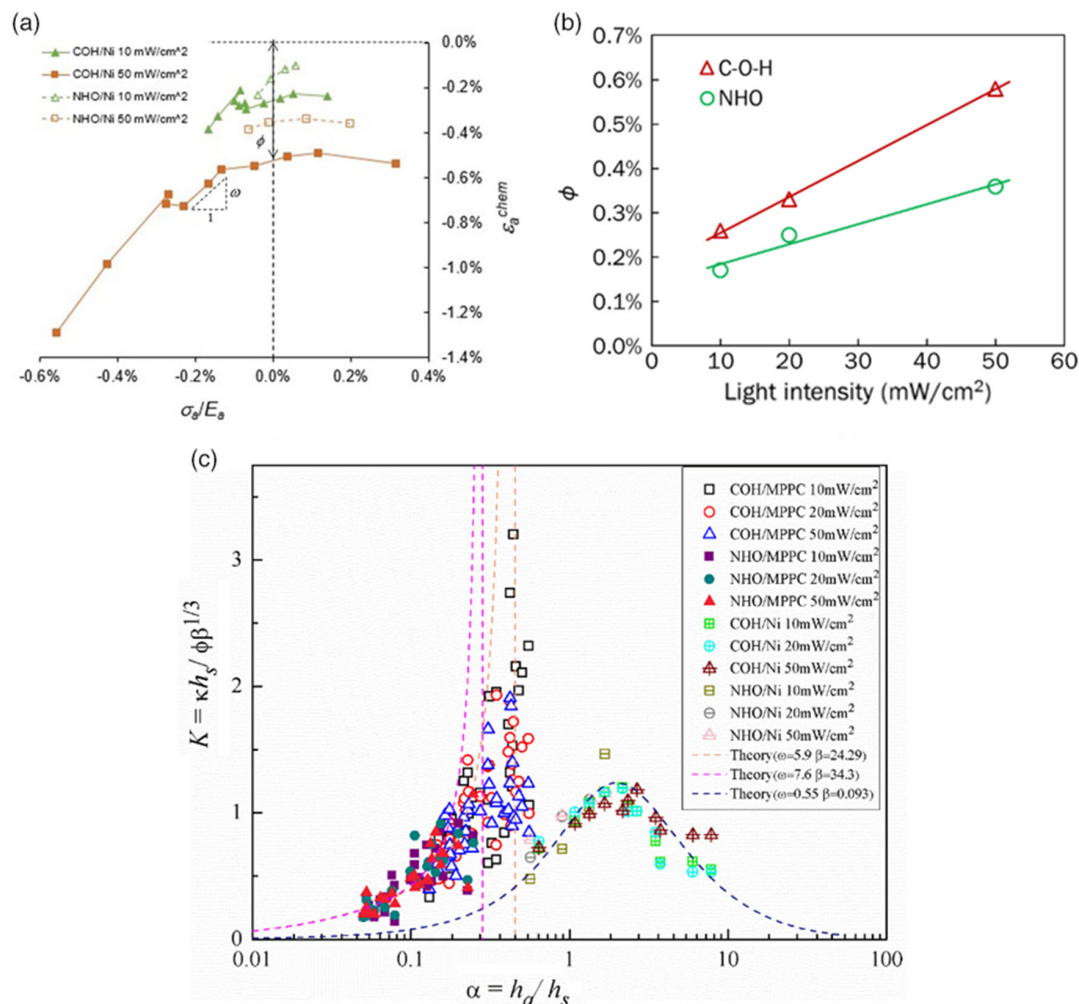


Figure 6. Intrinsic actuation responses. a) Plots of actuation stress and strain. Adapted with permission.^[65] Copyright 2019, Wiley-VCH. b) Normalized chemical driving force. Reproduced with permission.^[65] Copyright 2019, Wiley-VCH. c) Normalized comparison of different material systems. Reproduced with permission.^[72] Copyright 2020, Elsevier.

layers, as well as the activation energy and volume of the active material according to Equation (6). In other words, Equation (6) can be used to design actuators for specific actuation requirements.

4. Engineering Strategies for Device Design and Fabrication

To deploy turbostratic oxides/hydroxides in the abovementioned bimorph configuration, a number of enabling technologies developed are reviewed later.

4.1. Chemoelastic Instability

Equation (6) embodies a condition where the normalized curvature K can theoretically approach infinity, thus resulting in huge bending actuation of the bimorph configuration.^[72] As shown in Figure 5d, a large (plastic) contractive strain ϵ_a^{chem} within the active layer will cause the bimorph actuator to bend severely, thus establishing a compressive stress σ_a on the stimulated surface. The effective chemical force ($\Delta E_{\text{chem}} - \sigma_a \Omega$) for the stimulation therefore increases, driving the active layer further toward the contractive state to make ϵ_a^{chem} even more contractive. A situation of positive feedback therefore arises, causing the actuation to become unstably large. In Figure 5a, the instability occurs when the mechanics characteristics in Equation (4), now in the third quadrant of the $\sigma_a - \epsilon_a^{\text{chem}}$ plot as both σ_a and ϵ_a^{chem} are contractive, become parallel to the chemical characteristics in Equation (3) so that no solution for σ_a and ϵ_a^{chem} would exist; this condition arises when $-E_a C_a = \omega$. Further analysis shows that the quantity $-E_a C_a$ is lower-bounded by two regardless of the thickness and Young's modulus of the active and passive layers,^[72] and so in general, the instability can occur only when $\omega \geq 2$. In Figure 5b, ω is < 2 , and the $K(\alpha, \beta)$ surface is always well behaved without singularity; however, in Figure 5c, the condition for $\omega \geq 2$ is met and then K becomes singular on the curve $\beta\alpha^2(2\alpha + 3) = 1$ in the α - β domain.^[72]

The instability is also demonstrated in Figure 6c for the COH and NHO actuators on microporous polycarbonate (MPPC) substrates, for which ω is larger than 2. For these actuators, the K value becomes very large when the thickness ratio α is between ≈ 0.3 and 0.6 . However, for COH and NHO actuators made on nickel-film substrates, $\omega < 2$ and K do not exhibit instability. The chemomechanical instability here offers a means to design bimorph actuators with very large bending actuation; to do this, the following conditions should be met: 1) select a material system with $\omega > 2$ and a large value of ϕ , and 2) choose α and β to fall into the instability range by considering Equation (6).

4.2. Microriveting

The MPPC substrates shown in Figure 6c are a type of polycarbonate (PC) membranes with micron-sized through-thickness pores available commercially as desalination filters, which were found to be excellent substrates for bimorph actuators.^[66] As shown in Figure 6c, COH or NHO actuators made on MPPC substrates have $\omega > 2$, thus the chemomechanical instability

may occur to achieve large bending actuation. Why this is so is believed to be partly due to the heat insulation effect of PC, so photothermal effect of the light stimuli results in a larger activation volume for water deintercalation.^[72] However, while oxide/hydroxide materials electrodeposited on metal (nickel) substrates exhibit good adhesion to allow several thousands of bending actuation cycles without degradation,^[61,65,67] the intrinsic adhesion between oxides/hydroxides on polymers is weak. Therefore, compared with solid PC substrates, the micropores in the MPPC membranes offer an important function—during fabrication of the bimorph actuators, the active material is deposited into the pores to form microrivets, as shown in Figure 7a. For the NHO active material, deposition onto solid PC without pores does not result in a strongly adhered bimorph actuator, which exhibits negligible actuation with immediate delamination of the NHO coating (Figure 7b). Pore sizes of 0.2 – $3 \mu\text{m}$ in the MPPC substrate with longer deposition time of the active material result in better actuation, as shown in Figure 7b. Bimorph actuators made this way can also undergo several thousands of actuation cycles without showing significant degradation in performance.^[66]

4.3. On-Demand Robot Printing

A significant advantage of the turbostratic oxides/hydroxides as actuating materials is that they can be printed onto different metallized substrates by conventional bath electrodeposition and “open” electrodeposition. Masked electrodeposition in an electrolyte bath allows a single pattern of the active material to be printed on a substrate as a single electrode in one go. However, for more complicated designs with the demodularized muscle-skeletal approach mentioned in Section 1, the substrate as the skeletal body of the robot may need to be connected to different muscle groups that need to be of different active materials or stimulated independently. For such robots, the single-pattern, single-electrode requirement in the bath electrodeposition method will be too limiting. Conversely, the open electrodeposition method, illustrated in Figure 7c, allows muscle groups of different materials or on different electrodes on the substrate to be written independently. This method is slower than the bath method, but is more versatile. Figure 7c shows a tailor-made printer which delivers the electrolyte via a syringe needle to the required location on the substrate.^[66,73] Upon application of a potential bias between the needle and the metallized substrate, the electrodeposition reaction happens at the gap between the needle and the substrate, and programmed movement of the needle then allows a pattern of the active material to be printed on the substrate.

5. Examples of Demodularized Muscle-Skeletal Devices Built

Utilizing NHO, COH, CNH, and MnO_x , a series of robotic devices have been fabricated and demonstrated,^[61,63,65–67] and a few examples are shown in Figure 8. Figure 8a shows a device mimicking an untethered insect powered by visible light.^[61] Here, two strips of NHO were printed as actuating muscles on a folded nickel foil as the robot body. On receiving blinking

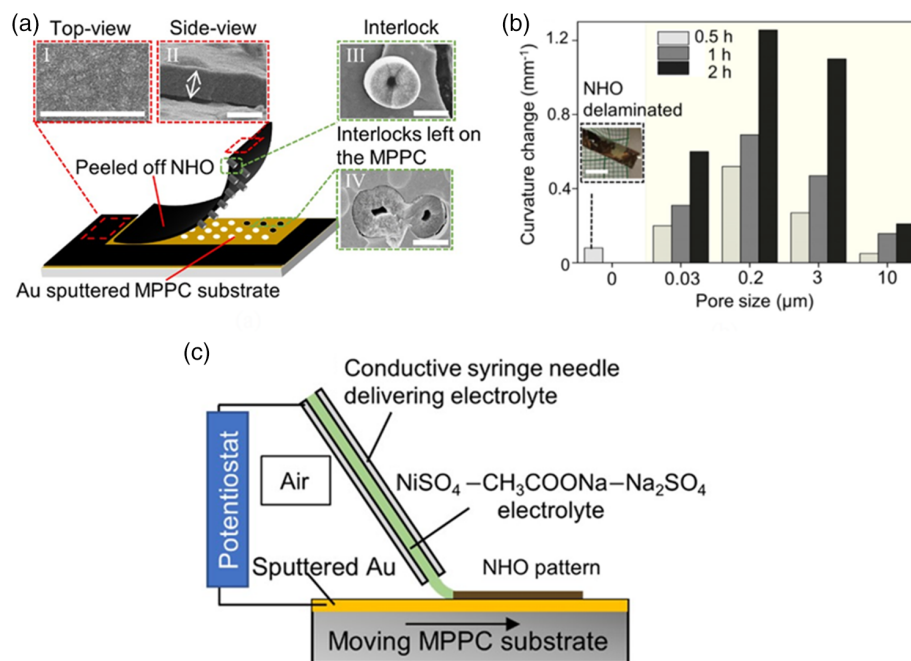


Figure 7. a,b) “Microriveting” for improving adhesion between active and passive layers in bimorph actuators. a) Schematic and scanning electron micrographs showing the microrivets on an NHO/MPPC actuator. b) Effects of pore size of the MPPC substrate, and deposition time (0.5, 1, or 2 h) of the NHO active material, on the bending curvature during electrochemical actuation. c) Direct writing of oxide materials on substrates by open electrodeposition, illustrating the example of NHO.^[73] a–c) Reproduced with permission.^[66] Copyright 2020, Elsevier.

light stimulation from a remote source, the illuminated NHO muscle actuates and recovers, causing a leg of the insect to fold and unfold. Due to the asymmetry of the friction with the ground, the insect crawls toward the light source. This application illustrates the concept of wireless delivery of power to a material-driven small-scale robot.

Figure 8b shows origami robots with active folding creases made by mask-patterned electrodeposition of NHO on MPPC substrates as the robot bodies.^[66] The robots are operable under electrochemical and light actuation as shown. Due to the demodularized muscle-skeletal architecture of the origami concept, very large device strains up to ≈60% are achievable.^[66]

Figure 8c shows an electrochemically actuated microhand with independently controlled finger joints made by direct writing of MnO_x on a flexible MPPC hand-shaped substrate coated with independent gold-sputtered electrodes.^[66] The MnO_x joints are independently controlled by connecting the Au electrodes to independent potential switches, enabling the hand to display different signals. As mentioned earlier, because of the multielectrode requirement, the finger joints in this application cannot be made by bath electrodeposition in one go, and this application illustrates the versatility of on-demand writing by the open-electrodeposition method in Figure 7c.

6. Outlook

The turbostratic oxides/hydroxides reviewed here are high-performing actuating materials that can be stimulated by multiple means, including light, electrochemical, heat, and

humidity signals. As shown in Table 1, these materials exhibit a holistically attractive set of actuation performances compared with existing materials. In terms of stimuli requirements, they need low potentials (<1 V) for electrochemical actuation, as similar to other electrochemical actuators such as CNTs and noble metals, and low intensities (<1 sun) in the visible range for light actuation, while other light actuators such as liquid-crystal elastomers require the UV regime in high intensities. Yet, the turbostratic oxides/hydroxides exhibit rather good actuation performances. Their stress range, in tens of MPa, is comparable with piezoelectric materials and conducting polymers, while their strain (≈1%), although falling short of the polymeric material systems, is rather high among inorganic materials. The response time of <1 s is also much faster compared with conducting and shape-memory polymers, or hydrogels. A particular benefit is their easy printability on various substrates, which is a key enabling factor for constructing robots with a demodularized muscle-skeletal architecture. Future work may focus on exploring other materials of this family, and the design methodology to integrate different actuating materials into the same device to achieve intelligent functionalities. The present oxides/hydroxides are usually printed as thin films on substrates to form bimorph actuators, but arising from their printability on different substrates, scaling up of the actuating capability may be possible by exploring 3D substrate constructs with a high compliance, say, those with a microporous architecture. As mentioned previously, of the various stimuli, light and electric signals are more readily delivered in a targeted manner than others such as heat, humidity, and magnetism, yet the electrochemical actuation of the present turbostratic oxides/

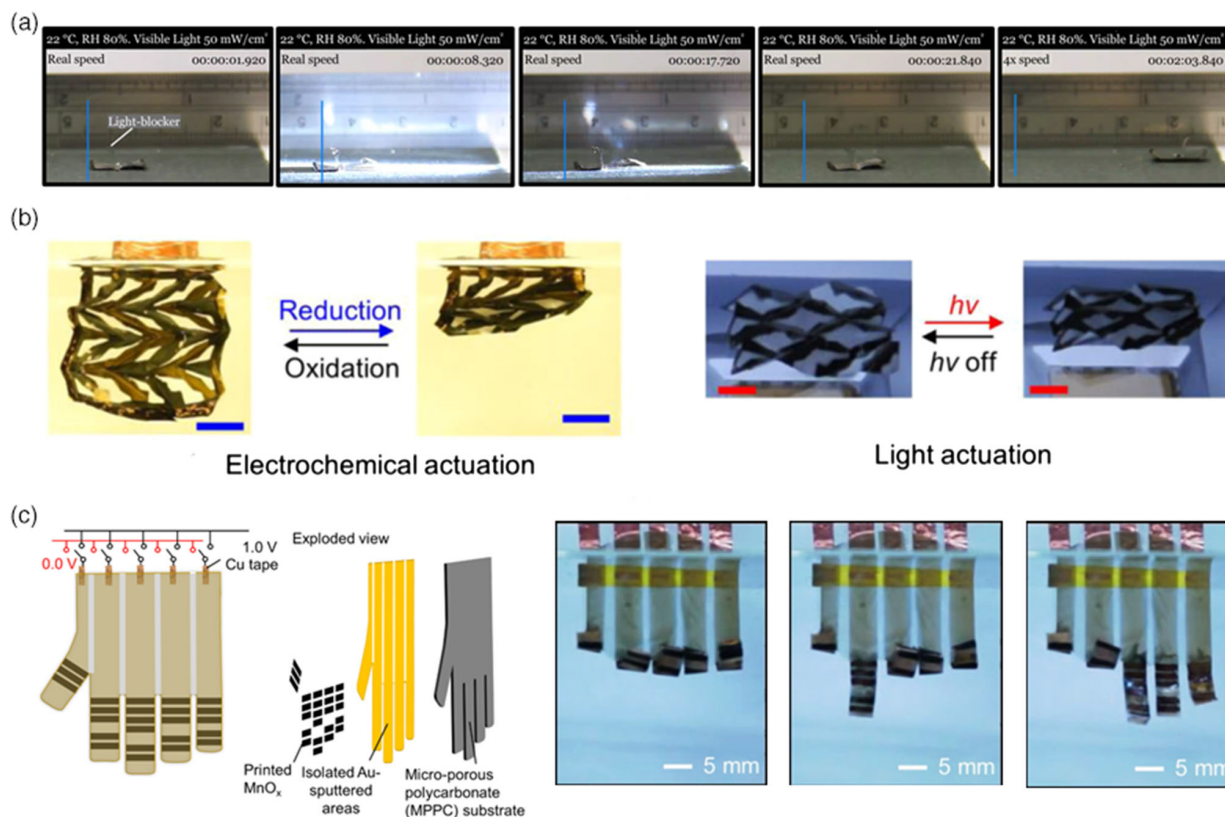


Figure 8. Exemplary robotic devices powered by turbostratic oxides/hydroxides. a) A robotic insect with NHO muscles on a nickel-foil substrate wirelessly powered by blinking light from a remote source on the right side. Actuation and recovery of muscle flexes the front leg to make the robot to crawl toward the light source. Adapted with permission.^[61] Copyright 2018, American Association for the Advancement of Science. b) Origami robots with NHO self-folding creases actuated electrochemically or by light. Reproduced with permission.^[66] Copyright 2020, Elsevier. c) Robotic hand with MnO_x finger joints independently controlled by electrochemical actuation. Adapted with permission.^[66] Copyright 2020, Elsevier.

hydroxides requires an electrolytic environment. However, the required electrolyte can be packaged in an actuator assembly for operation in a dry condition,^[63] and as future work, effective packaging methods can be studied. As mentioned, the oxide/hydroxide-based bimorph actuators studied in the past underwent thousands of actuation cycles without significant degradation, but longer term stability and effective means to achieve high adhesion strength between the active and passive layers need to be further investigated. Finally, in terms of the scientific basis of the actuation, the stimuli-induced water deintercalation mechanism is rather unknown at present. For instance, how the turbostraticity of oxides/hydroxides affects their chemical driving force ΔE_{chem} or ϕ , and activation volume Ω or ω , needs to be quantitatively understood.

Acknowledgements

This project was supported by a grant from the Innovation Technology Commission of the Hong Kong SAR Government (project code: PRP/061/19FX).

Conflict of Interest

The authors declare no conflict of interest.

Keywords

actuators, nickel hydroxide, printed robots, stimuli-responsive materials, turbostratic

Received: September 24, 2020
Revised: November 23, 2020
Published online: March 31, 2021

- [1] Q. M. Wang, Q. Zhang, B. Xu, R. Liu, L. E. Cross, *J. Appl. Phys.* **1999**, *86*, 3352.
- [2] Y. Saito, H. Takao, T. Tani, T. Nonoyama, K. Takatori, T. Homma, T. Nagaya, M. Nakamura, *Nature* **2004**, *432*, 84.
- [3] B. Jaffe, in *Piezoelectric Ceramics*, Vol. 3, Elsevier, Amsterdam **2012**, p. 27.
- [4] X. W. Dong, B. Wang, K. F. Wang, J. G. Wan, J. M. Liu, *Sens. Actuators A Phys.* **2009**, *A153*, 64.
- [5] B. Ameduri, *Chem. Rev.* **2009**, *109*, 6632.
- [6] Y. Tai, G. Lubineau, Z. Yang, *Adv. Mater.* **2016**, *28*, 4665.
- [7] B. Bera, M. D. Sarkar, *IOSR J. Appl. Phys.* **2017**, *9*, 95.
- [8] R. Pelrine, R. Kornbluh, J. Joseph, R. Heydt, Q. Pei, S. Chiba, *Mater. Sci. Eng. C*, **2000**, *11*, 89.
- [9] P. Brochu, Q. Pei, *Macromol. Rapid Commun.* **2010**, *31*, 10.
- [10] C. Keplinger, J.-Y. Sun, C. C. Foo, P. Rothermund, G. M. Whitesides, Z. Suo, *Science* **2013**, *341*, 984.

- [11] B. Chen, J. J. Lu, C. H. Yang, J. H. Yang, J. Zhou, Y. M. Chen, Z. Suo, *ACS Appl. Mater. Interfaces* **2014**, *6*, 7840.
- [12] B. Chen, Y. Bai, F. Xiang, J.-Y. Sun, Y. M. Chen, H. Wang, J. Zhou, Z. Suo, *J. Polym. Sci.* **2014**, *B52*, 1055.
- [13] T. F. Otero, H.-J. Grande, J. Rodriguez, *J. Phys. Chem.* **1997**, *B101*, 3688.
- [14] J. D. Madden, R. A. Cush, T. S. Kanigan, I. W. Hunter, *Synth. Met.* **2000**, *113*, 185.
- [15] L. Bay, K. West, P. Sommer-Larsen, S. Skaarup, M. Benslimane, *Adv. Mater.* **2003**, *15*, 310.
- [16] F. Garcia-Cordova, L. Valero, Y. A. Ismail, T. F. Otero, *J. Mater. Chem.* **2011**, *21*, 17265.
- [17] M. Hiraoka, P. Fiorini, J. O'Callaghan, I. Yamashita, C. Van Hoof, M. Op de Beek, *Sens. Actuators A Phys.* **2012**, *A177*, 23.
- [18] R. H. Baughman, C. Cui, A. A. Zakhidov, Z. Iqbal, J. N. Barisci, G. M. Spinks, G. G. Wallace, A. Mazzoldi, D. De Rossi, A. G. Rinzler, O. Jaschinski, S. Roth, M. Kertesz, *Science* **1999**, *284*, 1340.
- [19] T. Mirfakhrai, J. Oh, M. Kozlov, E. C.-W. Fok, M. Zhang, S. Fang, R. H. Baughman, J. D. W. Madden, *Smart Mater. Struct.* **2007**, *16*, S243.
- [20] J. Foroughi, J. Oh, M. Kozlov, S. Fang, T. Mirfakhrai, J. D. W. Madden, M. K. Shin, S. J. Kim, R. H. Baughman, *Science* **2011**, *334*, 494.
- [21] E. Wang, M. S. Desai, S.-W. Lee, *Nano Lett.* **2013**, *13*, 2826.
- [22] M. Ji, N. Jiang, J. Chang, J. Sun, *Adv. Funct. Mater.* **2014**, *24*, 5412.
- [23] J. Mu, C. Hou, H. Wang, Y. Li, Q. Zhang, M. Zhu, *Sci. Adv.* **2015**, *1*, e1500533.
- [24] H. Arazoe, D. Miyajima, K. Akaike, F. Araoka, E. Sato, T. Hikima, M. Kawamoto, T. Aida, *Nat. Mater.* **2016**, *15*, 1084.
- [25] Y. Hu, J. Liu, L. Chang, L. Yang, A. Xu, K. Qi, P. Lu, G. Wu, W. Chen, Y. Wu, *Adv. Funct. Mater.* **2017**, *27*, 1704388.
- [26] P. Zhou, L. Chen, L. Yao, M. Weng, W. Zhang, *Nanoscale* **2018**, *10*, 8422.
- [27] Q. Li, C. Liu, Y. H. Lin, L. Liu, K. Jiang, S. Fan, *ACS Nano* **2015**, *9*, 409.
- [28] Y. Hu, T. Lan, G. Wu, Z. Zhu, W. Chen, *Nanoscale* **2014**, *6*, 12703.
- [29] L. Chen, M. Weng, Z. Zhou, Y. Zhou, L. Zhang, J. Li, Z. Huang, W. Zhang, C. Liu, S. Fan, *ACS Nano* **2015**, *9*, 12189.
- [30] Y. Hu, G. Wu, T. Lan, J. Zhao, Y. Liu, W. Chen, *Adv. Mater.* **2015**, *27*, 7867.
- [31] M. Giorcelli, M. Bartoli, *Actuators* **2019**, *8*, 46.
- [32] J. Weissmüller, R. N. Viswanath, D. Kramer, P. Zimmer, R. Würschum, H. Gleiter, *Science* **2003**, *300*, 312.
- [33] D. Kramer, R. N. Viswanath, J. Weissmüller, *Nano Lett.* **2004**, *4*, 793.
- [34] R. N. Viswanath, D. Kramer, J. Weissmüller, *Electrochim. Acta* **2008**, *53*, 2757.
- [35] H. J. Jin, X. L. Wang, S. Parida, K. Wang, M. Seo, J. Weissmüller, *Nano Lett.* **2009**, *10*, 187.
- [36] E. Detsi, S. Punzhin, J. Rao, P. R. Onck, J. Th. M. De Hosson, *ACS Nano* **2012**, *6*, 3734.
- [37] Z. Zhao, J. Wu, X. Mu, H. Chen, H. J. Qi, D. Fang, *Macromol. Rapid Commun.* **2017**, *38*, 1600625.
- [38] Y. Mao, Z. Ding, C. Yuan, S. Ai, M. Isakov, J. Wu, T. Wang, M. L. Dunn, H. J. Qi, *Sci. Rep.* **2016**, *6*, 24761.
- [39] B. Jin, H. Song, R. Jiang, J. Song, Q. Zhao, T. Xie, *Sci. Adv.* **2018**, *4*, eaao3865.
- [40] Y. Cheng, K. Ren, D. Yang, J. Wei, *Sens. Actuators A* **2018**, *B255*, 3117.
- [41] H. Shigemune, S. Maeda, Y. Hara, N. Hosoya, S. Hashimoto, *IEEE/ASME Trans. Mech.* **2016**, *21*, 2746.
- [42] H. Meng, G. Li, *Polymer* **2013**, *54*, 2199.
- [43] M. Behl, A. Lendlein, *Mater. Today* **2007**, *10*, 20.
- [44] J. Karger-Kocsis, S. Keki, *Polymers* **2018**, *10*, 34.
- [45] C. De Marco, S. Pané, B. J. Nelson, *Sci. Robot.* **2018**, *3*, eaau0449.
- [46] G. Scalet, *Actuators* **2020**, *9*, 10.
- [47] J. Li, L. Mou, R. Zhang, J. Sun, R. Wang, B. An, H. Chen, K. Inoue, R. Ovalle-Robles, Z. Liu, *Carbon* **2019**, *148*, 487.
- [48] M. D. Lima, N. Li, M. J. de Andrade, S. Fang, J. Oh, G. M. Spinks, M. E. Kozlov, C. S. Haines, D. Suh, J. Foroughi, S. J. Kim, Y. Chen, T. Ware, M. K. Shin, L. D. Machado, A. F. Fonseca, J. D. W. Madden, W. E. Voit, D. S. Galvão, R. H. Baughman, *Science* **2012**, *338*, 928.
- [49] J. H. Na, A. A. Evans, J. Bae, M. C. Chiappelli, C. D. Santangelo, R. J. Lang, T. C. Hull, R. C. Hayward, *Adv. Mater.* **2015**, *27*, 79.
- [50] M. K. McBride, A. M. Martinez, L. Cox, M. Alim, K. Childress, M. Beiswinger, M. Podgorski, B. T. Worrell, J. Killgore, C. N. Bowman, *Sci. Adv.* **2018**, *4*, eaat4634.
- [51] Q. Ge, C. K. Dunn, H. J. Qi, M. L. Dunn, *Smart Mater. Struct.* **2014**, *23*, 094007.
- [52] K. Uchino, in *Advanced Piezoelectric Materials*, 2nd ed. (Ed. K. Uchino), Elsevier, Amsterdam **2017** pp. 755–785.
- [53] T.-C. Wei, H.-P. Wang, H.-J. Liu, D.-S. Tsai, J.-J. Ke, C.-L. Wu, Y.-P. Yin, Q. Zhan, G.-R. Lin, Y.-H. Chu, *Nat. Commun.* **2017**, *8*, 15018.
- [54] C. L. Van Oosten, C. W. Bastiaansen, D. J. Broer, *Nat. Mater.* **2009**, *8*, 677.
- [55] S. Iamsaard, *Nat. Chem.* **2014**, *6*, 229.
- [56] S. Petsch, R. Rix, B. Khatri, S. Schuhloden, P. Muller, R. Zentel, H. Zappe, *Sens. Actuators A* **2015**, *A231*, 44.
- [57] T. J. White, D. J. Broer, *Nat. Mater.* **2015**, *14*, 1087.
- [58] M. Lahikainen, H. Zeng, A. Priimagi, *Nat. Commun.* **2018**, *9*, 4148.
- [59] M. Dai, O. T. Picot, J. M. N. Verjans, L. T. De Haan, A. P. H. J. Schenning, T. Peijs, C. W. M. Bastiaansen, *ACS Appl. Mater. Interfaces* **2013**, *5*, 4945.
- [60] H. Lu, M. Zhang, Y. Yang, Q. Huang, T. Fukuda, Z. Wang, Y. Shen, *Nat. Commun.* **2018**, *9*, 3944.
- [61] K. W. Kwan, S. J. Li, N. Y. Hau, W. D. Li, S. P. Feng, A. H. W. Ngan, *Sci. Robot.* **2018**, *3*, eaat4051.
- [62] C. Cheng, A. H. W. Ngan, *ACS Nano* **2015**, *9*, 3984.
- [63] K. W. Kwan, N. Y. Hau, S. P. Feng, A. H. W. Ngan, *Sens. Actuators A* **2017**, *B248*, 657.
- [64] W. A. Sławiński, A. O. Sjästad, H. Fjellvåg, *Inorg. Chem.* **2016**, *55*, 12881.
- [65] K. W. Kwan, A. H. W. Ngan, *Adv. Mater. Tech.* **2019**, *4*, 1900746.
- [66] R. Wu, K. W. Kwan, W. Ma, P. Wang, A. H. W. Ngan, *Appl. Mater. Today* **2020**, *20*, 100621.
- [67] K. W. Kwan, A. H. W. Ngan, *ACS Appl. Mater. Interfaces* **2020**, *12*, 30557.
- [68] L. Liu, L. Su, Y. Lu, Q. Zhang, L. Zhang, S. Lei, S. Shi, M. D. Levi, X. Yan, *Adv. Funct. Mater.* **2019**, *29*, 1.
- [69] K. W. Kwan, D. G. Xie, R. R. Zhang, Z. W. Shan, A. H. W. Ngan, *Phys. Status Solidi* **2018**, *A215*, 1800623.
- [70] N. Arencibia, V. Oestreicher, F. A. Viva, M. Jobbágy, *RSC Adv.* **2017**, *7*, 5595.
- [71] D. Hung, V. Oestreicher, M. Mizrahi, F. G. Requejo, M. Jabbágy, *Chem. Eur. J.* **2020**, *26*, 1.
- [72] W. Ma, K. W. Kwan, R. Wu, A. H. W. Ngan, *Extreme Mech. Lett.* **2020**, *39*, 100801.
- [73] P. Wang, R. C. Roberts, A. H. W. Ngan, *Sci. Rep.* **2016**, *6*, 27423.
- [74] A. Van der Ven, D. Mrogan, Y. S. Meng, G. Ceder, *J. Electrochem. Soc.* **2006**, *153*, A210.
- [75] D. S. Hall, D. J. Lockwood, C. Bock, B. R. MacDougall, *Proc. R. Soc. A* **2015**, *471*, 20140792.
- [76] V. Yu. Kazimirov, M. B. Smirnov, L. Bourgeois, L. Guerlou-Demourgues, L. Servant, A. M. Balagurov, I. Natkaniec, N. R. Khasanova, E. V. Antipov, *Solid State Ion.* **2010**, *181*, 1764.



Kin Wa Kwan is a postdoctoral research fellow of Department of Mechanical Engineering, the University of Hong Kong. His research interests include actuating materials for artificial muscles. He obtained his bachelor, master, and Ph.D. degrees in engineering from the University of Hong Kong in 2010, 2011, and 2016, respectively.



Runni Wu is carrying out the postdoctoral research work at the University of Hong Kong. Her research interests include fabrication of actuators and the design of multifunctional actuating systems. She received bachelor and master degrees from Wuhan University in 2013 and 2016, and Ph.D. degree in mechanical engineering from the University of Hong Kong in 2020.



Wenrui Ma is a Ph.D. candidate in the Department of Mechanical Engineering, the University of Hong Kong. His research focuses on fabrication and characterization of multiresponsive actuating materials, and their engineering designs. He obtained his bachelor degree from Harbin Institute of Technology in 2018.



Alfonso H. W. Ngan is Kingboard Professor in materials engineering at the University of Hong Kong. His research interests include the microstructural basis of mechanical properties of materials, nanomechanics, and novel actuating materials. He obtained Ph.D. and D.Sc. degrees from Birmingham University, UK, in 1992 and 2008, respectively. He is elected Fellow of the Hong Kong Academy of Engineering Sciences, and the Institute of Materials, Minerals and Mining (IMMM) in the United Kingdom.